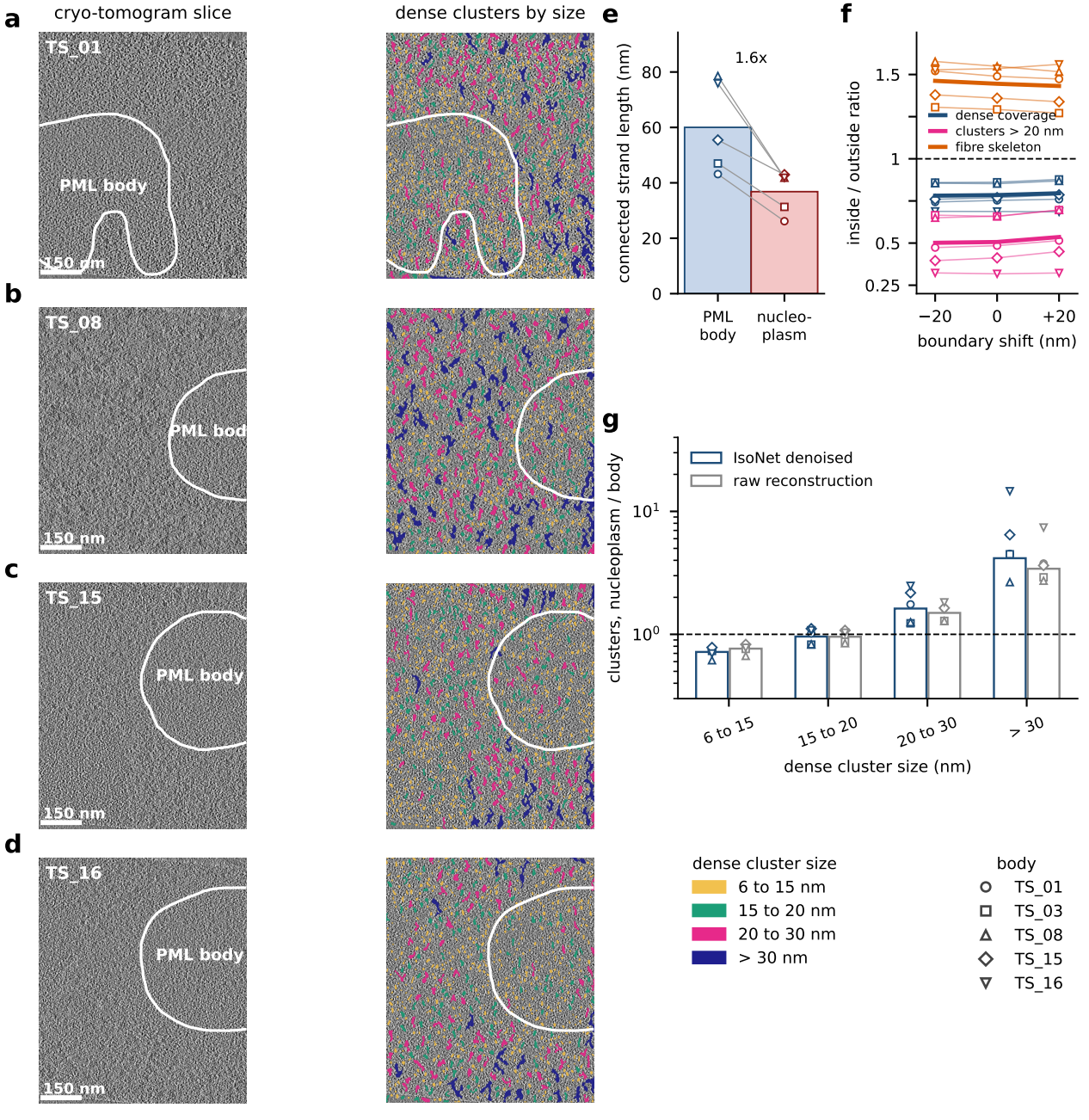
a
cryo-tomogram slice
dense clusters by size
TS_01
PML body
150 nm
b
TS_08
PML bod
150 nm
c
TS_15
PML body
150 nm
d
TS_16
PML body
150 nm
e
connected strand length (nm)
1.6x
PML body
nucleo-plasm
f
inside / outside ratio
dense coverage
clusters > 20 nm
fibre skeleton
boundary shift (nm)
g
clusters, nucleoplasm / body
IsoNet denoised
raw reconstruction
6 to 15
15 to 20
20 to 30
> 30
dense cluster size (nm)
dense cluster size
6 to 15 nm
15 to 20 nm
20 to 30 nm
> 30 nm
body
TS_01
TS_03
TS_08
TS_15
TS_16

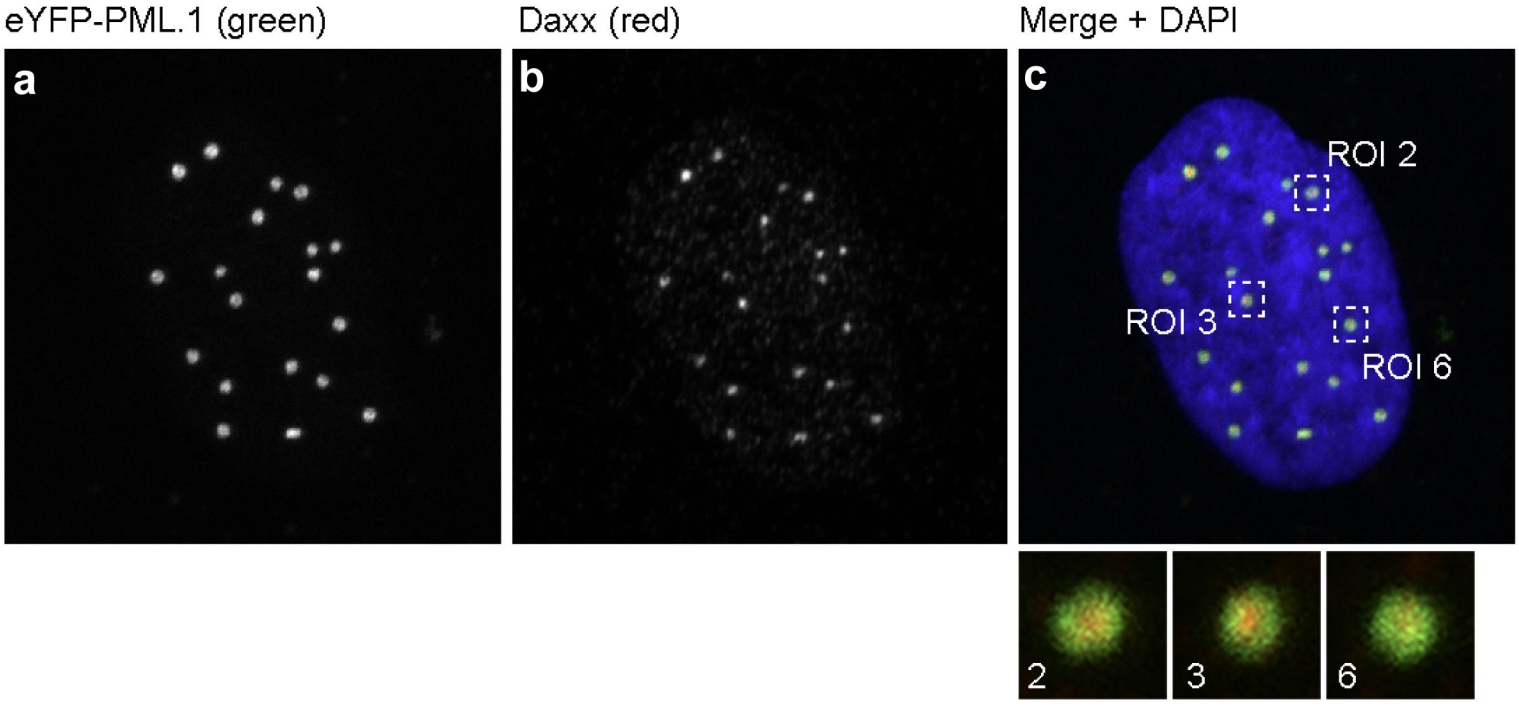


# Supplementary Fig. 2

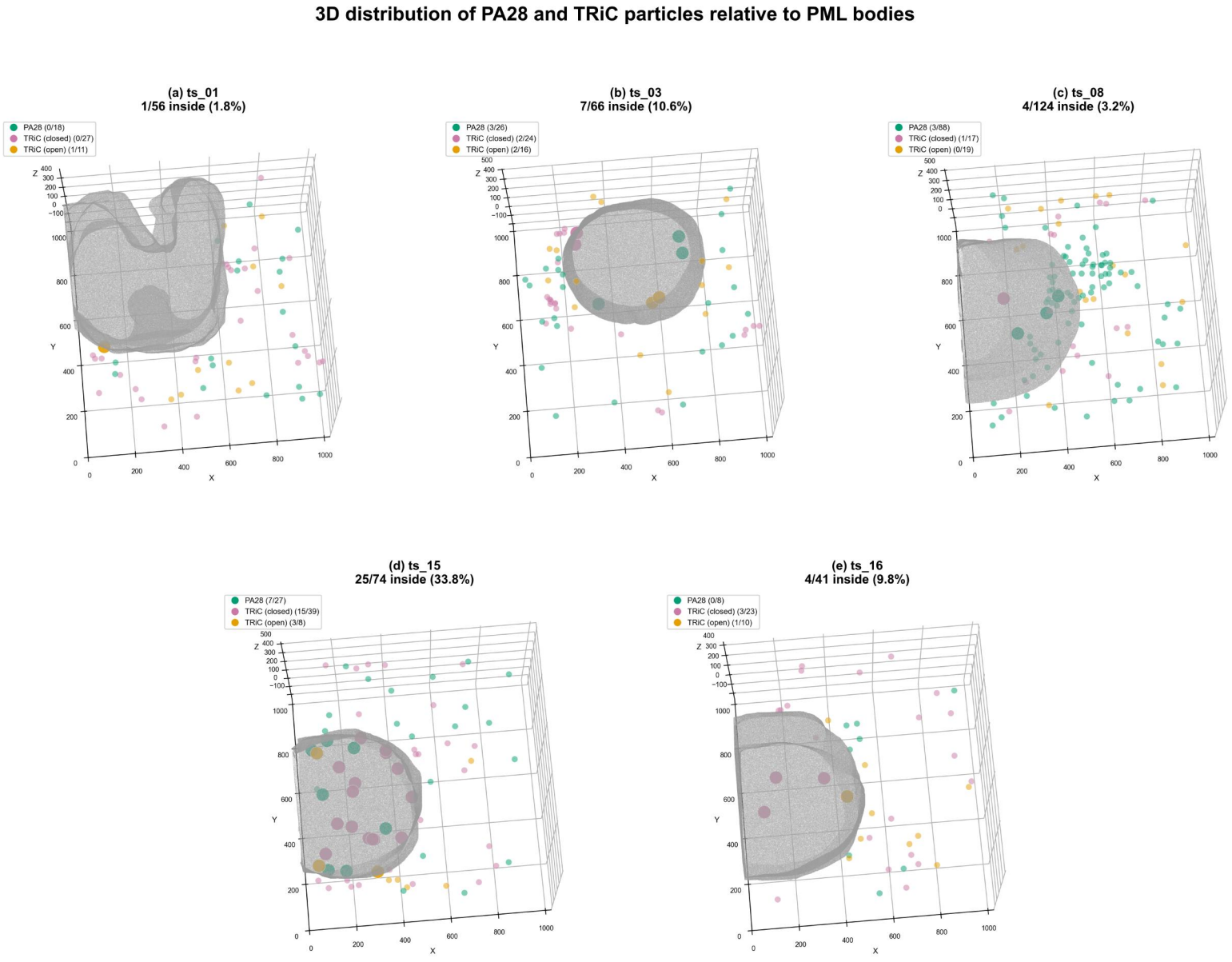


# Supplementary Fig. 3

**PA28 and TRiC particles inside vs outside PML bodies across five segmented tomograms**

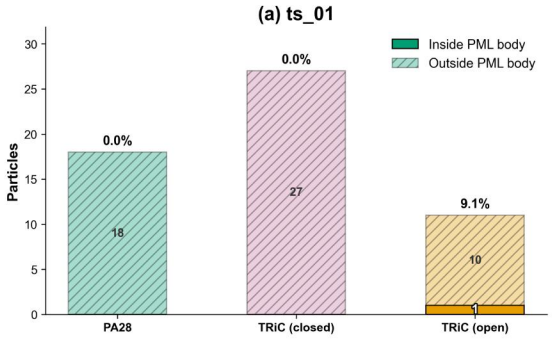


| Type | Total | In | Out | % In |
|---|---|---|---|---|
| PA28 | 18 | 0 | 18 | 0.0% |
| TRiC (closed) | 27 | 0 | 27 | 0.0% |
| TRiC (open) | 11 | 1 | 10 | 9.1% |
| TRiC (combined) | 38 | 1 | 37 | 2.6% |
| **All** | **56** | **1** | **55** | **1.8%** |

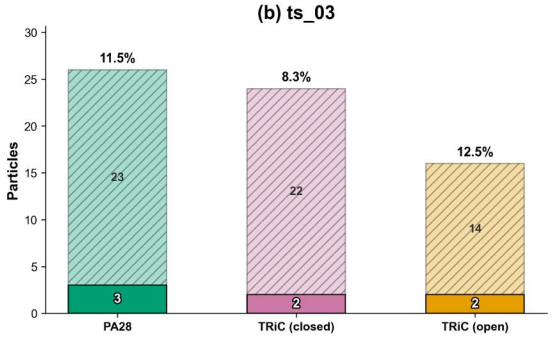


| Type | Total | In | Out | % In |
|---|---|---|---|---|
| PA28 | 26 | 3 | 23 | 11.5% |
| TRiC (closed) | 24 | 2 | 22 | 8.3% |
| TRiC (open) | 16 | 2 | 14 | 12.5% |
| TRiC (combined) | 40 | 4 | 36 | 10.0% |
| **All** | **66** | **7** | **59** | **10.6%** |

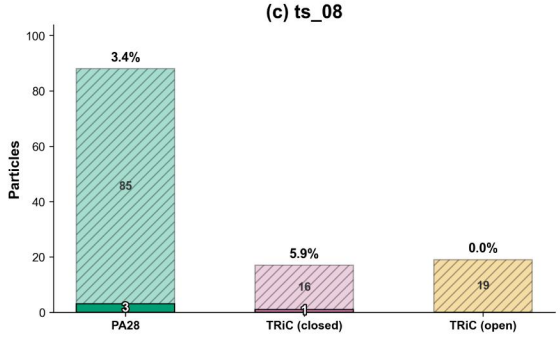


| Type | Total | In | Out | % In |
|---|---|---|---|---|
| PA28 | 88 | 3 | 85 | 3.4% |
| TRiC (closed) | 17 | 1 | 16 | 5.9% |
| TRiC (open) | 19 | 0 | 19 | 0.0% |
| TRiC (combined) | 36 | 1 | 35 | 2.8% |
| **All** | **124** | **4** | **120** | **3.2%** |

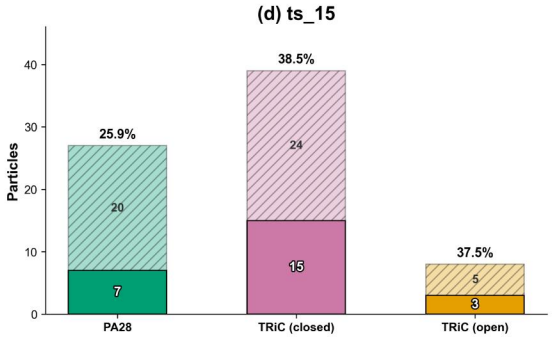


| Type | Total | In | Out | % In |
|---|---|---|---|---|
| PA28 | 27 | 7 | 20 | 25.9% |
| TRiC (closed) | 39 | 15 | 24 | 38.5% |
| TRiC (open) | 8 | 3 | 5 | 37.5% |
| TRiC (combined) | 47 | 18 | 29 | 38.3% |
| **All** | **74** | **25** | **49** | **33.8%** |

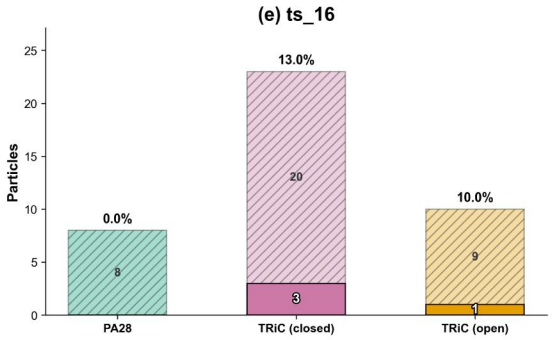


| Type | Total | In | Out | % In |
|---|---|---|---|---|
| PA28 | 8 | 0 | 8 | 0.0% |
| TRiC (closed) | 23 | 3 | 20 | 13.0% |
| TRiC (open) | 10 | 1 | 9 | 10.0% |
| TRiC (combined) | 33 | 4 | 29 | 12.1% |
| **All** | **41** | **4** | **37** | **9.8%** |

Supplementary Fig. 4

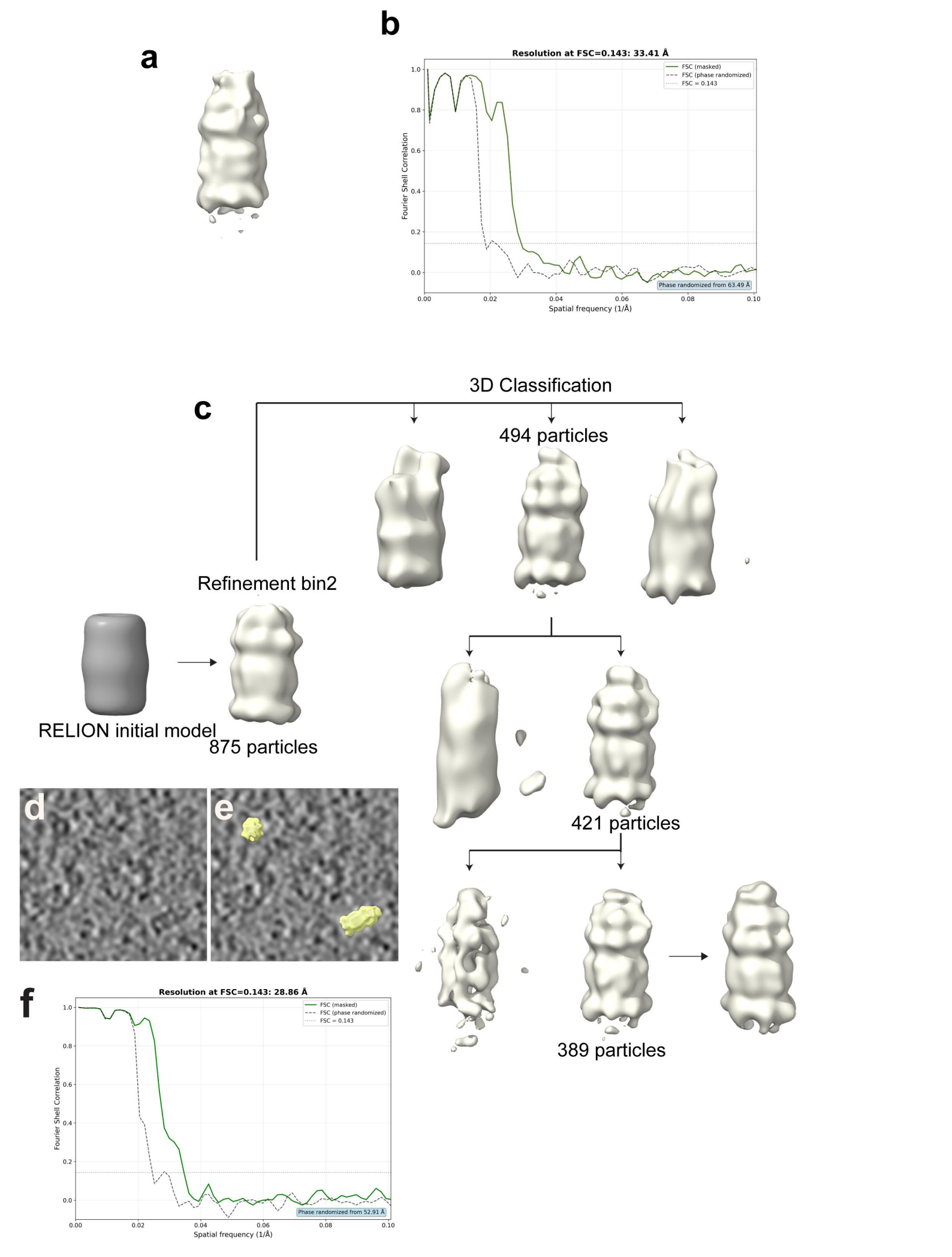


Supplementary Fig. 5

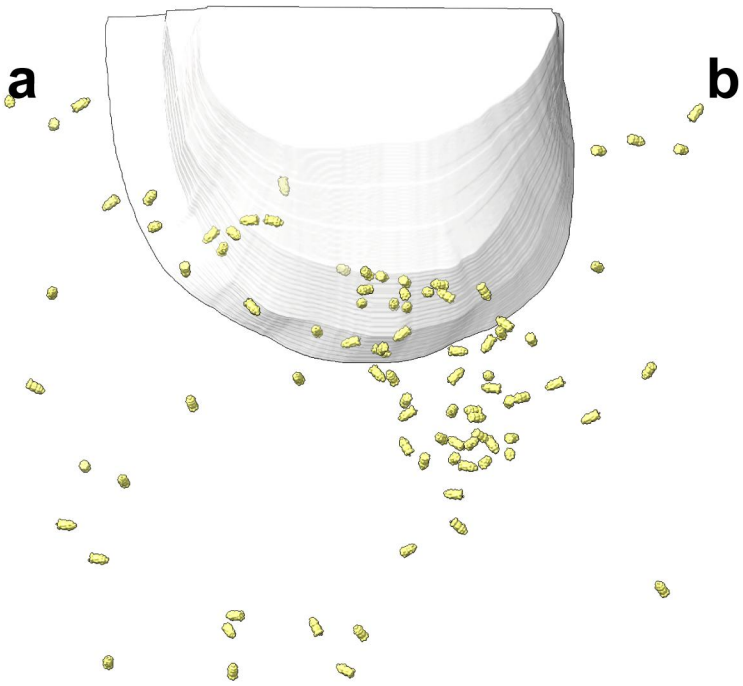


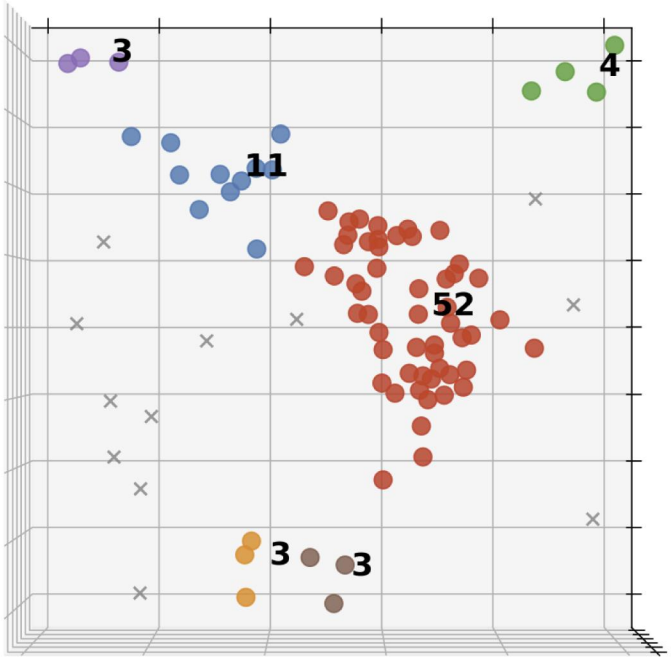


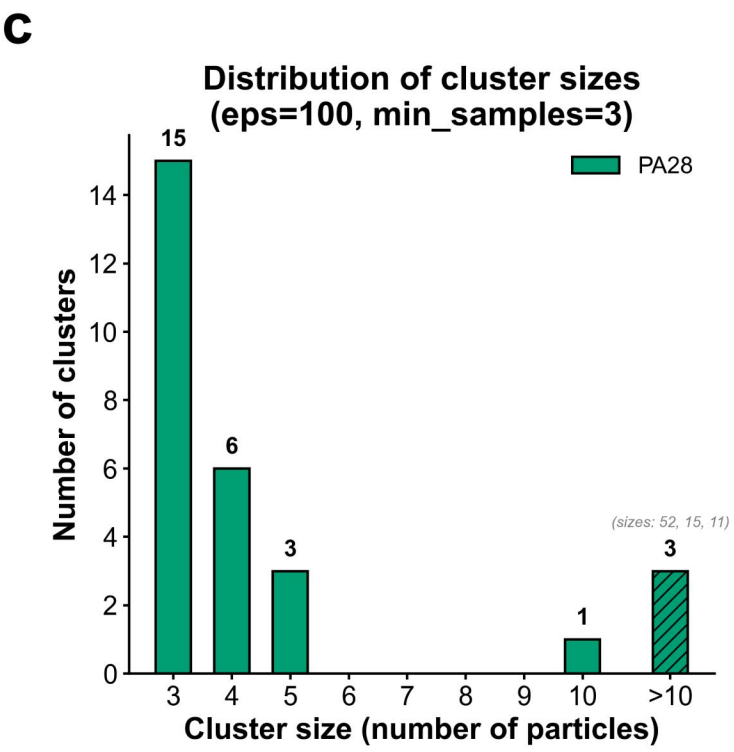


Supplementary Fig. 6




Supplementary Fig. 7

**Nucleosome and Trinucleosome Particles Inside vs Outside PML Bodies Across 5 Segmented Tomograms**

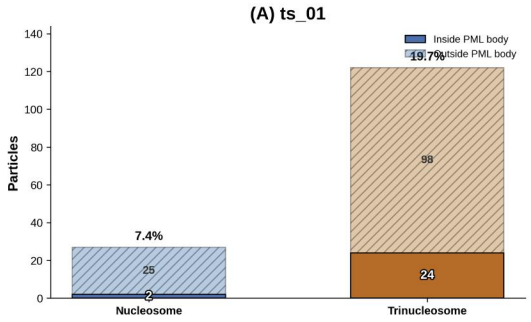


| Type | Tot | In | Out | %In |
|---|---|---|---|---|
| Nucleosome | 27 | 2 | 25 | 7.4% |
| Trinucleosome | 122 | 24 | 98 | 19.7% |
| **All** | **149** | **26** | **123** | **17.4%** |

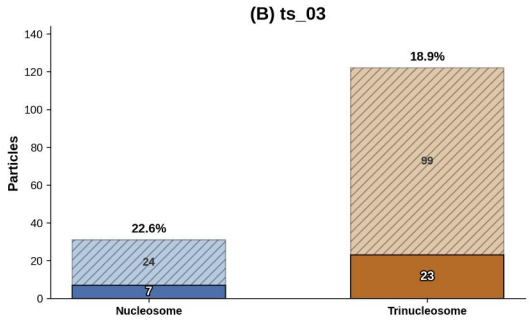


| Type | Tot | In | Out | %In |
|---|---|---|---|---|
| Nucleosome | 31 | 7 | 24 | 22.6% |
| Trinucleosome | 122 | 23 | 99 | 18.9% |
| **All** | **153** | **30** | **123** | **19.6%** |

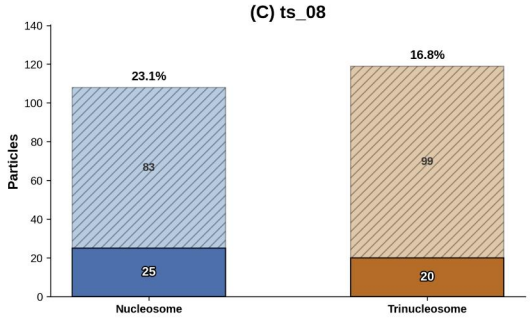


| Type | Tot | In | Out | %In |
|---|---|---|---|---|
| Nucleosome | 108 | 25 | 83 | 23.1% |
| Trinucleosome | 119 | 20 | 99 | 16.8% |
| **All** | **227** | **45** | **182** | **19.8%** |

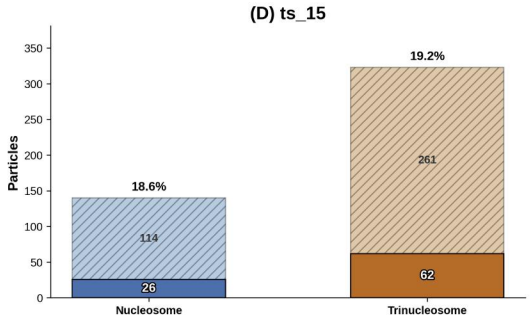


| Type | Tot | In | Out | %In |
|---|---|---|---|---|
| Nucleosome | 140 | 26 | 114 | 18.6% |
| Trinucleosome | 323 | 62 | 261 | 19.2% |
| **All** | **463** | **88** | **375** | **19.0%** |

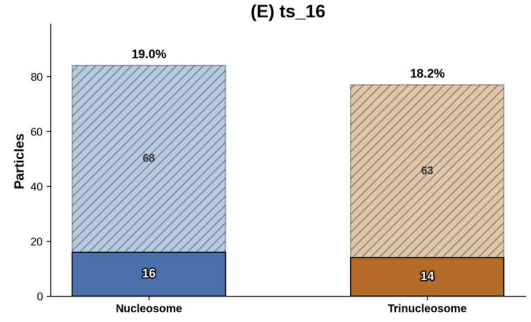


| Type | Tot | In | Out | %In |
|---|---|---|---|---|
| Nucleosome | 84 | 16 | 68 | 19.0% |
| Trinucleosome | 77 | 14 | 63 | 18.2% |
| **All** | **161** | **30** | **131** | **18.6%** |

# Supplementary Fig. 8

a

b

c

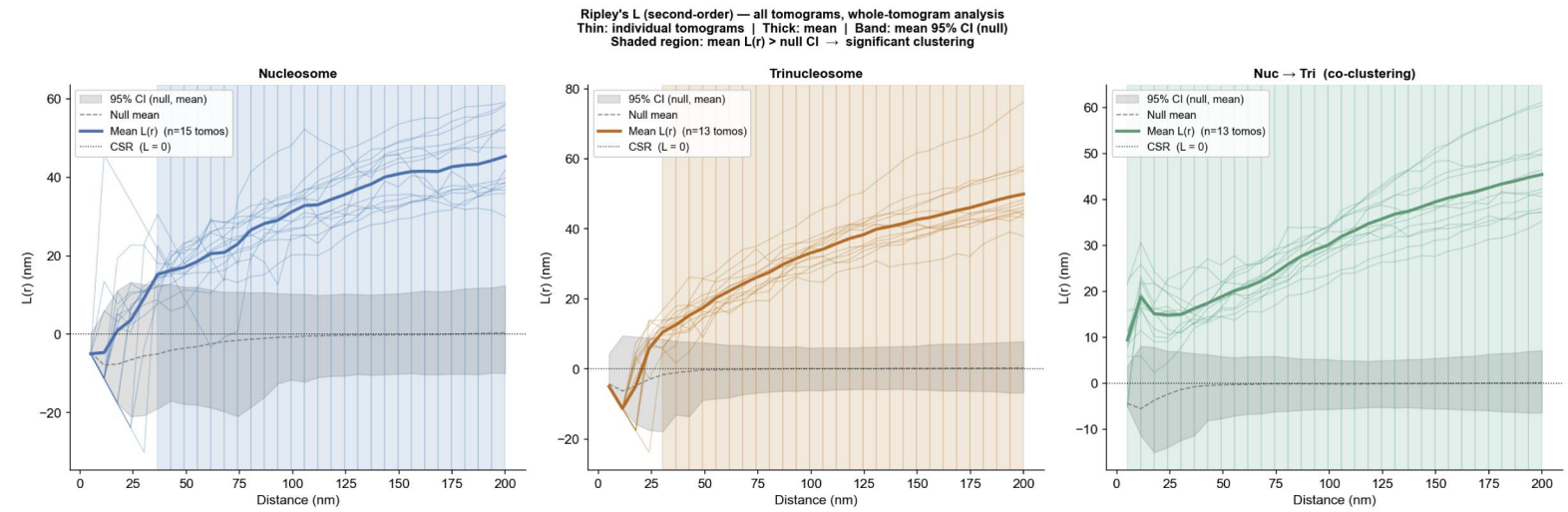


Supplementary Fig. 9

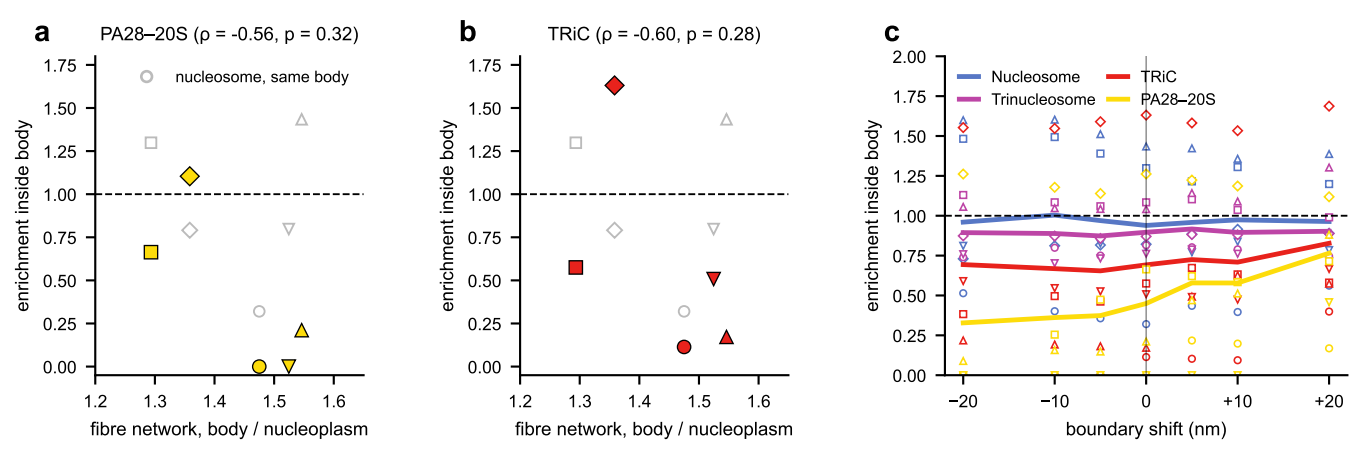
a
PA28–20S (ρ = -0.56, p = 0.32)
nucleosome, same body
enrichment inside body
fibre network, body / nucleoplasm
b
TRiC (ρ = -0.60, p = 0.28)
enrichment inside body
fibre network, body / nucleoplasm
c
Nucleosome
Trinucleosome
TRiC
PA28–20S
enrichment inside body
boundary shift (nm)

| Collection | Instrument | FIB source | Magnification | Lamellae prepared (n) | PML body tomograms (n) | Adjacent tomograms (n) |
|---|---|---|---|---|---|---|
| 1st | Arctis (Rosalind Franklin Institute) | Xe | 33,000× | 3 | 7 | — |
| 2nd | Arctis (Rosalind Franklin Institute) | Xe | 53,000× | 3 | 3 | 9 |
| 3rd | Arctis (Rosalind Franklin Institute) | Ar | 53,000× | 7 | 17 | 9 |
| **Total** | | | | **13** | **27** | **18** |

# Supplementary Table 1

| Dataset ID | Cryo-tomogram category | Lamellae Thickness (nm) | Distance from PML-YFP fluorescence in x,y (nm) |
|---|---|---|---|
| TS_01 | PML-YFP cryo-fluorescence captured | 220 | / |
| TS_03 | PML-YFP cryo-fluorescence captured | 200 | / |
| TS_04 | PML-YFP cryo-fluorescence captured | 206 | / |
| TS_08 | PML-YFP cryo-fluorescence captured | 181 | / |
| TS_15 | PML-YFP cryo-fluorescence captured | 230 | / |
| TS_16 | PML-YFP cryo-fluorescence captured | 230 | / |
| TS_162 | PML-YFP cryo-fluorescence captured | 212 | / |
| TS_17 | Nucleoplasm | 215 | 2051 |
| TS_32 | Nucleoplasm | 210 | 2906 |
| TS_43 | Nucleoplasm | 227 | 3856 |
| TS_52 | Nucleoplasm | 134 | 789 |
| TS_82 | Nucleoplasm | 174 | 3798 |
| TS_83 | Nucleoplasm | 190 | 1000 |
| TS_132 | Nucleoplasm | 160 | 1366 |
| TS_142 | Nucleoplasm | 225 | 1419 |
| TS_152 | Nucleoplasm | 206 | 1932 |

# Supplementary Table 2

**Supplementary Table 3. Summary of template matching parameters and results.**

| Target complex | Template description | Template (EMDB/PDB) | Conformation | LP filter (Å) | Initial detections (n) | Into RELION 4.0 (n) | After 3D class. (n) | STA resolution (Å) |
|---|---|---|---|---|---|---|---|---|
| **TRiC chaperonin** | TRiC closed state | EMDB-18913 | Closed | 40 | 378 | 335[a] | 297 | 22 |
| | TRiC open state | EMDB-18921 | Open | 40 | 580 | 413[a] | 276 | 32 |
| **Proteasome** | 20S core particle (Phase 3) | EMDB-4877 | Core only | 40 | 1,468 | 580[b] | — | — |
| | PA28 single-capped (Phase 2) | EMDB-30824 | Single-capped | 40 | 1,659 | 566[c] | 538 | 33 |
| | PA28 single-capped (Phase 3) | EMDB-30824 | Single-capped | 40 | — | 875[d] | 389 | 28.86 |
| | PA200 single-capped | EMDB-24278 | Single-capped | 40 | 2,335 | — | —* | — |
| | PA28 double-capped | EMDB-24277 | Double-capped | 40 | 213 | — | — | — |
| | PA200 double-capped | EMDB-4860 | Double-capped | 40 | 362 | — | — | — |
| | 19S single-capped | EMDB-4002 | Single-capped | 40 | 402 | — | — | — |
| | 19S double-capped | EMDB-9512 | Double-capped | 40 | 1,356 | — | — | — |
| **Nucleosome** | Nucleosome core particle | EMDB-8140 | — | 40 | 22,680 | 5,517[e] | 957[f] | 19 |
| **Trinucleosome** | Trinucleosome (original) | PDB-7V9S | Open state | 40 | 2,821 | 2,821 | 2,287[g] | 25/19[h] |
| | Trinucleosome (hole-modified) | Modified from PDB-7V9S | Open state (val.) | 40 | 1,769 | — | — | — |

[a] After CC-score competition for overlapping positions: 335 closed and 413 open TRiC particles assigned to RELION 4.0; 3D classification yielded 297 closed and 276 open final maps.
[b] Phase 3: 20S core-only positions (not co-localising with any cap template within 10 nm) after overlap grouping of 3,935 unique positions; 580 input to RELION 4.0 as reference anchor; not subjected to independent STA.
[c] Phase 2: multi-step validation pipeline (overlap grouping → CC-ranked cap assignment → cap–core co-localisation within 10 nm + Y-axis orientation filter); 566 particles input to RELION 4.0; 538 retained after 3D classification (T = 2, 3 classes), STA at 33 Å.
[d] Phase 3: simplified two-template approach — PA28 detections retained only if co-localising with a 20S core within 10 nm (orientation filter omitted); 875 particles input to RELION 4.0, refined by 3D classification to 389 final particles at 28.86 Å.
* PA200 single-capped: STA produced uninterpretable density, consistent with false-positive cross-matching; not pursued further.
[e] Threshold-filtered (+0.03 above mean LCC 0.519) from 22,680 initial detections; all 5,517 input to RELION 4.0 for STA (19 Å map).
[f] Particles retained after iterative 3D classification in RELION 4.0 (nucleosome core particle class; 19 Å reconstruction).
[g] 2,821 particles input to RELION 4.0; 2,287 retained after 3D classification, used for both global (25 Å) and focused (19 Å) STA and for DBSCAN analysis across 13 tomograms.
Dual-template validation (original + hole-modified 7V9S) yielded 1,371 overlapping particles with consistent Y-axis orientations (mean angular deviation 8.9°).
[h] 25 Å for full trinucleosome map; 19 Å for focused refinement on top nucleosome subunit.
LP, low-pass filter; STA, subtomogram averaging; —, not applicable.

*Summary of template matching parameters and results for all complexes searched by PyTOM template matching within eYFP-PML-I cryo-tomograms.*

**Supplementary Information**

# In situ architecture of PML nuclear bodies reveals a porous, chromatin-permissive interior

Vojtěch Pražák1,2, Iain Harley3,4, Julian Falckenhayn1,5, Chris Boutell3, Peter A. Thomason4, Benjamin G. Davis6,7,8, Rainer Kaufmann1,5, Stephen D. Carter3,4 *

## Contents

Supplementary Note 1

Supplementary Figs. 1–10

Supplementary Tables 1–3

Legends for Supplementary Videos 1–12

## Supplementary Note 1 | PA28 single-capped proteasome identification by multi-template matching

Seven proteasome-related templates were used for template matching in PyTOM: the 20S core particle (EMDB-4877), single-capped PA28 (EMDB-30824), single-capped PA200 (EMDB-24278), double-capped PA28 (EMDB-24277), double-capped PA200 (EMDB-4860), single-capped 19S (EMDB-4002), and double-capped 19S (EMDB-9512). All templates were pre-aligned in ChimeraX so that the 20S barrel lay along Z and the cap(s) pointed in the same direction, allowing Euler angles from different templates to be directly compared. Template matching across all 16 tomograms yielded 7,795 initial detections: 20S Core (1,468), PA28 (1,659), PA200 (2,335), 19S-Single (402), 19S-Double (1,356), PA28-Double (213), and PA200-Double (362). CC score analysis indicated that 19S templates yielded lower scores than PA28, PA200, and 20S Core detections, while double-capped templates showed comparable scores but substantially fewer detections (Extended Data Fig. 4a).

We applied spatial overlap analysis (10 nm tolerance) to group the 7,795 detections into 3,935 unique positions (many detected by more than one template), then used CC-ranked cap assignment to determine the proteasome species at each position, excluding 20S Core detections from the competition. Double-capped templates produced zero winners and 19S templates contributed fewer than 1% of winners, indicating these species were not detected in any of the 16 cryo-tomograms (Extended Data Fig. 4c).

To validate cap assignments, we required that each cap detection spatially overlap with a 20S Core particle within 10 nm, and that the cap-Core Y-axis angle was either aligned (< 40°) or flipped (> 140°), consistent with cap binding to either end of the 20S barrel

(Extended Data Fig. 4b). The orientation filter confirmed the biological validity of the detections: across all inter-template overlapping pairs (n = 8,605), 52.4% fell within the aligned range and 46.5% within the flipped range. Since all templates were aligned with the cap pointing in the same direction, the symmetry of the 20S core barrel means template matching detects it equally in both orientations, producing the observed ~50/50 split between aligned and flipped cap positions, with only 1.1% falling outside these ranges (Extended Data Fig. 4b).

To recover genuine PA28 proteasomes, we required each cap detection to spatially overlap with a 20S Core detection within 10 nm (Phase 3; Extended Data Fig. 4c). This two-template filter yielded 875 validated PA28 single-capped proteasome particles and 580 unpaired Core-only detections. STA of the validated PA28 set in RELION 4.0 with iterative 3D classification yielded a final reconstruction of 389 particles at 29 Å resolution (Fig. 3n–p; Supplementary Fig. 5c–f), with clear densities for both the 20S core barrel and the PA28 cap.

**Supplementary Figures**

**Supplementary Fig. 1 |** Dense clusters and fibre network in the other four PML-I bodies. a–d, Central slices through TS_01 (a), TS_08 (b), TS_15 (c) and TS_16 (d), each shown as the cryo-tomogram slice (left) and with dense clusters coloured by equivalent diameter (right); white outline, cryo-CLEM body boundary. Scale bars, 150 nm. e, Mean length of connected skeleton strands inside the body and in the nucleoplasm after masking all dense clusters, five bodies (symbols as in Fig. 2c); strands were 1.6 fold longer inside. f, Sensitivity of the inside to outside ratios of dense coverage, clusters larger than 20 nm and fibre skeleton density to the position of the cryo-CLEM boundary, recomputed with the boundary eroded (negative shift) or dilated (positive shift) by 20 nm; thin lines, individual bodies (symbols as in Fig. 2c); thick lines, five body means; dashed line, ratio of 1. g, Nucleoplasm to body ratio of dense cluster density per size class on the IsoNet denoised reconstructions and on the raw AreTomo2 reconstructions, five body means. Analysis as in Fig. 2 and Methods.

**Supplementary Fig. 2 | Daxx immunofluorescence as a positive control for PML body colocalisation.** a, eYFP-PML-I channel (green) showing eYFP-PML-I nuclear bodies. b, Daxx immunofluorescence (red), a known PML body component. c, Merged image with DAPI (blue) showing colocalisation of eYFP-PML-I and Daxx signals. Insets show magnified ROIs 2, 3, and 6, confirming Daxx colocalisation with PML bodies.

**Supplementary Fig. 3 | 3D distribution of PA28 and TRiC particles relative to PML-I bodies.** a–e, 3D renderings of PML body segmentations from five tomograms (a, TS_01; b, TS_03; c, TS_08; d, TS_15; e, TS_16), showing the spatial distribution of PA28 (green), TRiC closed (pink), and TRiC open (orange) particles. PML body surface meshes (grey, semi-transparent) were segmented in Amira and rendered using isosurface extraction via marching cubes. Large spheres indicate particles classified as

inside the PML body, small spheres indicate particles outside. Inside/outside classification was performed using ray-casting on the triangulated mesh surface. Coordinates were scaled to bin4 pixel space (divide by 4) to match the segmentation volumes. Z-axis exaggeration (1.2x) and tilt corrections (25 deg X-tilt, 10 deg Y-tilt) were applied to better visualise the plots in 3D.

**Supplementary Fig. 4 | Quantification of PA28 and TRiC particle localisation within PML-I bodies.** a–e, Stacked bar charts and summary tables for each segmented tomogram (a, TS_01; b, TS_03; c, TS_08; d, TS_15; e, TS_16) showing the number of PA28, TRiC (closed), and TRiC (open) particles classified as inside (solid bars) or outside (hatched bars) the PML body. Percentages above each bar indicate the fraction of particles located within the PML body for each particle type. Summary tables list total, inside, and outside particle counts, with a combined TRiC row (closed + open) and an aggregate total.

**Supplementary Fig. 5 | PA28 single-capped proteasome STA.** a, STA map of PA28 single-capped proteasomes derived from Phase 2 of the workflow shown in Extended Data Fig. 4. b, Fourier shell correlation (FSC) curve for the PA28 Phase 2 STA, showing a resolution of 33 Å at the 0.143 criterion. c, STA pipeline for Phase 3 PA28 core-only overlaps. A *de novo* initial model was generated from 875 particles in RELION 4.0 and refined at bin2. Iterative 3D classification selected 494 particles, followed by further classification to 421 particles, and a final classification round yielding a best class of 389 particles. d, Cryo-tomogram slice showing two PA28 single-capped proteasomes. e, Same slice with PA28 particles highlighted in yellow. f, FSC curve for the PA28 single-capped proteasome STA, yielding a resolution of 29 Å at FSC=0.143.

**Supplementary Fig. 6 | PA28 single-capped proteasome spatial distribution relative to the PML-I body.** a, PA28 single-capped proteasome STAs (yellow) mapped onto the Amira-generated PML-I body mesh surface (white), showing the spatial distribution of PA28 particles relative to the PML-I body. b, DBSCAN clustering of PA28 particles in three dimensions, with cluster sizes indicated. c, Histogram showing the distribution of DBSCAN cluster sizes for PA28 particles (eps = 100 bin4 pixels (~99 nm), min_samples = 3). The majority of clusters contain 3–5 particles, with three larger clusters exceeding 10 particles (sizes: 52, 15, 11), indicating that PA28 particles form predominantly small, spatially dispersed clusters.

**Supplementary Fig. 7 | 3D distribution of nucleosome and trinucleosome particles relative to PML nuclear bodies.** a–e, 3D renderings of PML body segmentations from five tomograms (a, TS_01; b, TS_03; c, TS_08; d, TS_15; e, TS_16), showing the spatial distribution of nucleosome (blue) and trinucleosome (vermillion) particles. PML body surface meshes (grey, semi-transparent) were segmented in Amira and rendered using isosurface extraction via marching cubes. Particle positions are from the refined STA particle sets and are displayed as spheres; large markers indicate particles classified as inside the PML body, small markers indicate particles outside.

**Supplementary Fig. 8 | Quantification of nucleosome and trinucleosome particle localisation within PML nuclear bodies.** a–e, Stacked bar charts and summary tables for each segmented tomogram (a, TS_01; b, TS_03; c, TS_08; d, TS_15; e, TS_16) showing the number of nucleosome and trinucleosome particles classified as inside (solid bars) or outside (hatched bars) the PML body. Percentages above each bar indicate the fraction of particles located within the PML body for each particle type.

**Supplementary Fig. 9 | Ripley's L function analysis of nucleosome and trinucleosome spatial clustering.** Second-order Ripley's L(r) for (a) nucleosomes (n = 15 tomograms), (b) trinucleosomes (n = 13 tomograms), and (c) bivariate nucleosome–trinucleosome co-clustering (n = 13 tomograms). Thick lines show the mean L(r); thin lines show individual tomograms. Grey band: 95% confidence interval of the null model (complete spatial randomness, CSR; 200 Monte Carlo simulations per tomogram). Coloured shading marks radii at which the mean L(r) lies above the null band. L(r) exceeded its own null envelope in every tomogram: 15/15 (a), 13/13 (b, c).

**Supplementary Fig. 10 | Per body relation between fibre network density and particle enrichment, and sensitivity of enrichment to the body boundary.** a, b, Enrichment of PA28 single-capped proteasomes (a) and TRiC (b) inside each segmented body against the fibre network density of that body (body to nucleoplasm ratio, Fig. 2f); grey open symbols, nucleosome enrichment in the same body; symbols as in Fig. 2c; dashed line, enrichment of 1; Spearman rank correlation across the five bodies given in the panel titles. c, Enrichment of each particle type after eroding (negative) or dilating (positive) the segmented boundary by 5, 10 and 20 nm; thick lines, pooled over the five bodies; symbols, individual bodies. Particles were counted by voxel lookup in the shifted label volume, so the values at zero shift differ slightly from the mesh-based counts in Fig. 5 (PA28 14 of 167 against 13 of 167). Enrichment is the observed inside fraction divided by the fraction of the searched volume occupied by the body (see Methods).

## Supplementary Tables

**Supplementary Table 1 | Summary of cryo-pFIB lamella data collection.** Summary of cryo-pFIB lamella data collection across three sessions, detailing the instrument, pFIB plasma source, magnification, number of lamellae prepared, and PML body and adjacent nuclear tomograms collected per session.

**Supplementary Table 2 | Summary of the 16 cryo-tomogram datasets selected for analysis.** Table summarising the 16 cryo-tomogram datasets selected for analysis, with eYFP-PML-I cryo-fluorescence captured cryo-tomograms listed first (pink). Columns indicate the dataset ID, cryo-tomogram category, lamella thickness (nm), and distance from eYFP-PML-I fluorescence signal in x,y (nm). "/" denotes tomograms in which an

eYFP-PML-I body was directly captured within the field of view. Nucleoplasm datasets (blue) were collected from nuclear regions not containing a captured eYFP-PML-I body.

**Supplementary Table 3 | Summary of template matching parameters and results.** Summary of all template matching searches performed in PyTOM and subsequent STA workflow in RELION 4.0, including template descriptions, initial detection counts, particles carried into RELION 4.0, particles retained after 3D classification, and final STA resolution.

**Supplementary Videos**

**Supplementary Video 1 |** Particles identified by template matching and refined in RELION 4.0, mapped back onto the cryo-tomogram (TS_01) and coloured by type as in Fig. 3q (closed TRiC, red; open TRiC, light blue; PA28 single-capped proteasome, yellow; trinucleosomes, magenta; nucleosomes, blue). The white isosurface represents the segmented PML body. The closed-TRiC cluster is also visible (Fig. 3r–t).

**Supplementary Video 2 |** PyTOM cross-correlation score map for the closed TRiC template (EMDB-18913) overlaid onto a cryo-tomogram (TS_03). The template-matching score map was thresholded at a cross-correlation value of 0.47. The highest-scoring peaks coincide with high-contrast densities consistent with closed TRiC chaperonin complexes.

**Supplementary Video 3 |** PyTOM cross-correlation score map for the open TRiC template (EMDB-18921) overlaid onto a cryo-tomogram. The template-matching score map was thresholded at a cross-correlation value of 0.48. The highest-scoring peaks coincide with high-contrast densities consistent with open TRiC chaperonin complexes.

**Supplementary Video 4 |** PyTOM cross-correlation score map for the single-capped PA28 template (EMDB-30824) overlaid onto a cryo-tomogram. The template-matching score map was thresholded at a cross-correlation value of 0.40. The highest-scoring peaks coincide with high-contrast densities consistent with PA28-capped 20S proteasome complexes.

**Supplementary Video 5 |** PyTOM cross-correlation score map for the nucleosome template (EMDB-8140) overlaid onto a cryo-tomogram. The template-matching score map was thresholded at a cross-correlation value of 0.58. The highest-scoring peaks coincide with high-contrast densities consistent with nucleosome core particles.

**Supplementary Video 6 |** PyTOM cross-correlation score map for the open trinucleosome template (PDB-7V9S) overlaid onto a cryo-tomogram. The template-matching score map was thresholded at a cross-correlation value of 0.44. The highest-scoring peaks coincide with high-contrast multinucleosome assemblies.

**Supplementary Video 7 |** PyTOM cross-correlation score map for the open trinucleosome template (PDB-7V9S) overlaid onto a cryo-tomogram (TS_02). The template-matching score map was thresholded at a cross-correlation value of 0.48. The highest-scoring peaks coincide with high-contrast multinucleosome assemblies.

**Supplementary Video 8 |** PyTOM cross-correlation score map for the open trinucleosome template (PDB-7V9S) overlaid onto a cryo-tomogram (TS_52). The template-matching score map was thresholded at a cross-correlation value of 0.42. The highest-scoring peaks coincide with high-contrast multinucleosome assemblies.

**Supplementary Video 9 |** Particles identified by template matching and refined in RELION 4.0, mapped back onto the cryo-tomogram (TS_03) and coloured by type as in Fig. 3q (closed TRiC, red; open TRiC, light blue; PA28 single-capped proteasome, yellow; trinucleosomes, magenta; nucleosomes, blue). The white isosurface represents the segmented PML body. The closed-TRiC cluster is shown (Fig. 2a).

**Supplementary Video 10 |** Subtomogram average map of the nucleosome core particle at 19 Å resolution, rendered transparent with PDB 2CV5 fitted into the density and shown rotating, as in Fig. 4a–c.

**Supplementary Video 11 |** Nucleosome and open trinucleosome particles refined in RELION 4.0, mapped back onto the cryo-tomogram (TS_15), as in Fig. 4e,f. Nucleosomes are shown in blue and open trinucleosomes in magenta. The white isosurface represents the segmented PML body.

**Supplementary Video 12 |** Subtomogram average map of the open trinucleosome rendered transparent with PDB 7V9S fitted into the density and shown rotating, as in Fig. 4h,i.